PAPER

Atomistic simulations of dynamics of an edge dislocation and its interaction with a void in copper: a comparative study

To cite this article: Wu-Rong Jian *et al* 2020 *Modelling Simul. Mater. Sci. Eng.* **28** 045004

IOP Publishing Modelling and Simulation in Materials Science and Engineering

Modelling Simul. Mater. Sci. Eng. **28** (2020) 045004 (20pp) https://doi.org/10.1088/1361-651X/ab8358

Atomistic simulations of dynamics of an edge dislocation and its interaction with a void in copper: a comparative study

Wu-Rong Jian[1], Min Zhang[2], Shuozhi Xu[3] and Irene J. Beyerlein[1,3,4]

[1] Department of Mechanical Engineering, University of California, Santa Barbara, Santa Barbara, California 93106-5070, United States of America
[2] School of Materials Science and Engineering, University of Science and Technology Beijing, Beijing, 100083, People's Republic of China
[3] California NanoSystems Institute, University of California, Santa Barbara, Santa Barbara, California 93106-6105, United States of America
[4] Materials Department, University of California, Santa Barbara, Santa Barbara, California 93106-5050, United States of America

E-mail: wurong@ucsb.edu

Received 26 November 2019, revised 6 March 2020
Accepted for publication 25 March 2020
Published 27 April 2020

Abstract

Atomistic simulation methods are appropriate tools for investigating the dynamics of dislocations and their interactions with obstacles in metallic materials. In particular, molecular dynamics (MD) simulations have been widely employed on these two topics in the past several decades. However, even for the same type of simulation, the results can vary. While some of the quantitative differences may be due to the choices of interatomic potential and simulation cell size, they could similarly be attributed to choice of model settings, which have also differed substantially to date. In this paper, we carry out systematic MD simulations to study the effects of a few key model settings on the dynamics of an edge dislocation and its interaction with a void in copper. For a fixed interatomic potential, three modeling parameters, including applied loading mode, boundary conditions, and thermostat, are considered and their influences on the stress–strain response, the dislocation velocity, and the critical stress for a dislocation to bypass a void are compared. For a few select cases, we further examine the influence of temperature, strain rate, and simulation cell size. The results show that (i) compared with flexible boundary conditions, rigid boundary conditions result in greater stress oscillations in simulation cells of certain sizes; (ii) compared with the cases of no thermostat and a full thermostat, a partial

thermostat provides better temperature control and lower friction on the dislocation core, respectively; and (iii) for dislocation–void interactions, the critical dislocation bypassing stress in shear loading can be appropriately determined with either a constant applied strain rate or a constant applied stress although the strain rate cannot be controlled in the latter. This analysis reveals that these three settings greatly influence the accuracy and interpretation of the results for the same type of simulation.

Keywords: loading mode, boundary condition, thermostat, dislocation dynamics, dislocation–void interaction, atomistic simulations

(Some figures may appear in colour only in the online journal)

1. Introduction

Dislocations are the main carriers of plasticity in metals [1]. To examine dislocations in motion, scientists have developed several *in situ* experimental methods [2, 3], such as transmission electron microscopy [4] and x-ray topographic characterization [5]. Through these experimental techniques, the movement of dislocations can be observed directly or characterized indirectly. However, it is still difficult to acquire certain data in experiments, such as driving force and dislocation velocity, as well as the effects of obstacle sizes and density on dislocation motion. As a complement to direct observation, considerable insight into these quantities have been obtained via atomic-level calculations [6, 7]. Molecular dynamics (MD) simulation method is one such approach.

MD simulations have been utilized widely to identify the role of dislocation motion, interactions, and reactions in basic processes, such as the grain boundary (GB) migration [8–12], twinning [13–15], and dislocation nucleation from GBs [16–19] and voids [20, 21]. In particular, MD simulations are indispensable for our understanding of the dynamics of a dislocation [22, 23], providing insights into phonon scattering [24] and energy radiation [25] caused by the glide of dislocations in a lattice. Via MD simulations, researchers measured dislocation mobility in face-centered cubic (FCC) [26–32], body-centered cubic (BCC) [25, 33–36] and hexagonal close-packed (HCP) [37–39] metals. MD simulations are also carried out to explain the interactions between dislocations and different obstacles, such as dislocation–void interaction [40–43], dislocation–precipitate interaction [44–47] and dislocation–GB interaction [48–51].

In many of the MD simulations mentioned above, researchers utilized various model settings, choices usually driven by technical development or particular research goals. For example, over the years, newer formulations of interatomic potentials for copper have been tested via investigations of dislocation dynamics [43, 52–55]. Among these interatomic potentials, the intrinsic stacking fault energy varies, leading to discrepancies associated with dissociated core width, mobility, and reactions involving dislocations. Simulation cell size is another important factor. Due to the rapid improvements in the computational capacity, the size effect on dislocation dynamics has been frequently examined [29, 56]. Other model settings, including loading mode, boundary condition (BC), and thermostat, can also greatly differ among MD studies. To drive dislocation motion, for example, there are two main loading modes, differing in whether the applied strain rate or the applied stress is kept constant [22, 57]. The former mode has been used primarily to study dislocation–obstacle interactions [58–60], while the latter is adopted to measure dislocation mobility [26, 29, 31]. For shear loading with constant applied strain rate, four BCs were mainly employed, i.e., rigid, linear-rigid,

semi-rigid and flexible BCs [22, 57, 61]. For shear loading with constant applied stress, the super-particle-rigid BC is usually applied [22, 57]. Besides the loading mode and BC, another important parameter choice is whether or not a thermostat is applied and if so, which type. Cho *et al* [31] and Dang *et al* [62] considered that any thermostat may introduce artifact frictional forces to atoms in the dislocation core region, and hence interfere dislocation dynamics. However, a thermostat is still widely used in the literature [29, 55]. Like the first two factors (interatomic potential and simulation cell size), these three model settings could affect predictions on dislocation dynamics and dislocation–void interactions. For example, Rodney [61] found that the stress peak-to-peak amplitudes for a dislocation gliding in a lattice are 300 MPa and 100 MPa when the non-flexible and the flexible BCs, respectively, are used. To the best of our knowledge, the effects of these model settings have yet to be systematically quantified.

In this work, we utilize large-scale MD simulations to investigate the effects of three model parameters—loading mode, BC, and thermostat—on the dynamics of an edge dislocation and its interaction with a void in copper. In select cases, we also analyze the effects of the temperature, strain rate, and simulation cell size. The suitability of these parameters is assessed by the amplitude of oscillations in the stress–strain response, temperature variation with time, dislocation motion, and critical stress for a dislocation to bypass a void. In most cases, we find that a shear loading simulation with (i) constant applied strain rate, (ii) flexible BC, (iii) partial thermostat, and (iv) strain rates lower than 10^7 s^{-1} provides the best combination of modeling parameters. Although these factors have been individually studied in aforementioned atomistic simulations, it is the first time, to our best knowledge, to systematically investigate all of them in the context of the same problem. In addition, some investigations in our work are novel, including applying flexible boundary condition to dislocation–obstacle interaction and analyzing the effect of aspect ratio on the stress–strain response of pure dislocation motion without dislocation bow-out.

2. Methodology

Large-scale Atomic/Molecular Massively Parallel Simulator (LAMMPS) [63] is utilized in our MD simulations. To describe the atomic interactions in copper, we choose the embedded-atom method (EAM) potential proposed by Mishin *et al* [64], which has been widely applied in MD simulations of dislocations and stacking fault formation in copper [28, 55, 65–69].

The schematic in figure 1 presents the model setup for simulating dislocation mobility and dislocation–void interactions. The $[1\bar{1}0]$, $[11\bar{2}]$ and [111] crystallographic directions in a face centered cubic (FCC) copper single crystal are parallel to the x-, y- and z-axes, respectively. Periodic BCs are imposed along the x- and y-axes, while non-periodic BCs are present along the z-axis. Following references [22, 57], an edge dislocation is inserted by joining two half crystals on the (111) plane, with the top half crystal having two more $[1\bar{1}0]$ atomic planes than the bottom one. To minimize the system energy, the conjugate gradient algorithm is applied, causing the dislocation to dissociate. Minimization iterations are terminated when one of the following criteria is satisfied [70, 71]: (1) the energy change between successive iterations divided by the energy magnitude is less than or equal to 10^{-12} or (2) the length of the global force vector for all atoms is less than or equal to 10^{-12} eV $Å^{-1}$.

Next dynamic relaxation is conducted. First, we randomly assign velocities to all atoms following a Gaussian distribution to produce an initial temperature T. Unless stated otherwise, $T = 1$ K. In select cases, $T = 300$ K. In view of the thermal expansion at finite temperature, an NPT ensemble is applied to the whole cell. Since the NPT ensemble cannot

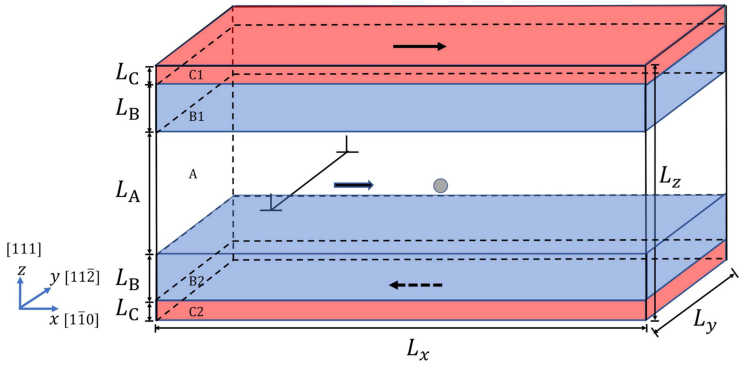

Figure 1. Schematic of the MD simulation cell. The whole cell is divided into A, B1, B2, C1, and C2 blocks, where different ensembles may be applied. Meanwhile, BCs are imposed in C1 and C2. '⊥' denotes the dissociated edge dislocation, while a void with 2 nm in diameter is on its right. For shear loading with constant applied strain rate, a velocity along the positive x direction is applied to C1, while C2 is usually fixed. For shear loading with constant applied stress, two equal but opposite forces along the x direction are superimposed in atoms in C1 and C2, respectively.

be utilized with non-periodic BC, the BC along the z-axis is made periodic until relaxation has completed. We then create two vacuum regions above the top surface and below the bottom surface, respectively. It should be noted the vacuum regions are used only in the relaxation step, and not in energy minimization or subsequent dynamic shear loading. For the dislocation–void interaction simulations, a void 2 nm in diameter is additionally carved on the right of the edge dislocation just after the energy minimization. In all dynamic simulations, either dynamic relaxation or subsequent dynamic shear loading, the timestep size is 1 fs.

After achieving the equilibrium atomic configuration via dynamic relaxation, the two vacuum regions are removed and the BC along the z direction is changed back to non-periodic. In preparation for the subsequent dynamic shear loading, we divide the entire simulation cell into five regions, i.e., A, B1, B2, C1 and C2, as illustrated in figure 1. Different BCs may be applied to C1 and C2, while different thermostats may be used in A, B1, and B2. The thicknesses of C1 and C2 along the z direction are the same and denoted as L_C. Similarly, the thicknesses of B1 and B2 are equal and referred to as L_B. Note that L_C should exceed the cutoff distance of the interatomic potential, i.e., 5.5 Å in the current work, to ensure that atoms in A, B1, and B2 are not affected by the non-periodic BCs [72, 73]. Hence, each of the C1 and C2 regions includes four layers of atoms. The ratio of the thickness of region A to that of the entire cell, i.e., L_A/L_z, is about 0.6, and the remaining thickness equals $2L_B$, where L_x, L_y, and L_z, are the edge lengths along the x-, y-, and z-axes, respectively.

In what follows, the temperature-related, the interatomic potential-induced, and the applied atomic velocities will be designated as $\mathbf{v}^T$, $\mathbf{v}^P$, and $\mathbf{v}^A$, respectively. Also we denote the interatomic potential-induced and the applied atomic forces as $\mathbf{f}^P$ and $\mathbf{f}^A$, respectively. As such, the atomic velocities $\mathbf{v} = \mathbf{v}^T + \mathbf{v}^P + \mathbf{v}^A$, and the atomic forces $\mathbf{f} = \mathbf{f}^P + \mathbf{f}^A$. We consider two loading modes: constant applied strain rate and constant applied stress. For the constant applied strain rate mode, four BCs, namely, rigid, linear-rigid, semi-rigid and flexible BCs are applied to C1 and C2, as summarized in table 1. In the rigid BC [53], $\mathbf{v}$

Table 1. Atomic velocity, force, and relaxation for atoms in regions C1 and C2 in different BCs. We set $z = 0$ at the bottom of the simulation cell along the z direction. Unless stated otherwise, the atomic velocity and force are uniform to all atoms in the specific region. We use 'null' to represent no control over velocities or forces along that direction.

BC	Direction	Velocity (C1)	Velocity (C2)	Force (C1 & C2)	Relaxation (C1 & C2)
Rigid	x	v_x^{A}	0	0	No
	y	0	0	0	No
	z	0	0	0	No
Linear-rigid	x	$v_x^{\mathrm{A}} z/L_z$	0	0	No
	y	0	0	0	No
	z	0	0	0	No
Semi-rigid	x	v_x^{A}	0	0	No
	y	Null	Null	Null	Yes
	z	Null	Null	Null	Yes
Flexible	x	Average v_x^{A}	Average 0	Total 0	Yes
	y	Null	Null	Null	Yes
	z	Null	Null	Null	Yes
Super-particle	x	$v_x^{\mathrm{P}} + v_x^{\mathrm{T}}$	$v_x^{\mathrm{P}} + v_x^{\mathrm{T}}$	$f_x^{\mathrm{P}} + f_x^{\mathrm{A}}$	Yes
	y	$v_y^{\mathrm{P}} + v_y^{\mathrm{T}}$	$v_y^{\mathrm{P}} + v_y^{\mathrm{T}}$	f_y^{P}	Yes
	z	$v_z^{\mathrm{P}} + v_z^{\mathrm{T}}$	$v_z^{\mathrm{P}} + v_z^{\mathrm{T}}$	f_z^{P}	Yes

and **f** of atoms in C1 and C2 are first zeroed, and then a constant velocity along the positive x direction, v_x^{A}, is applied to C1. Consequently, a constant applied strain rate $\dot{\gamma} = v_x^{\mathrm{A}}/(L_z - 2L_{\mathrm{C}})$ is achieved. The linear-rigid BC [22, 61] is similar to the rigid BC, except that the velocity in the C1 region varies linearly along the z direction. In this BC, the applied velocity of the top-most atomic layer in C1 is v_x^{A}, while the applied atomic velocity decreases linearly with distance from v_x^{A} in the top-most layer to $v_x^{\mathrm{A}}(L_z - L_{\mathrm{C}})/L_z$ in the bottom-most atomic layer in C1. Compared with the rigid BC, the semi-rigid BC [39] only zeroes v_x and f_x in C1 and C2, such that the atoms therein are free to move along the y and z directions.

In the foregoing three BCs, the interatomic distances within the same xy layer in C1 or C2 are unchanged along all directions (rigid BC and linear-rigid BC) or along the x direction (semi-rigid BC). To allow for changes in the interatomic distances in C1 and C2 (and hence relaxation of the atoms within), Rodney [61] proposed the flexible BC. In this BC, the average velocities along the x direction of all atoms in C1 and C2 are first calculated, as v_x^{C1} and v_x^{C2}, respectively. Then two opposite-signed velocities, $-v_x^{\mathrm{C1}}$ and $-v_x^{\mathrm{C2}}$, are uniformly added to all atoms in the two regions, respectively. Similarly, the total forces along the x direction of all atoms in C1 and C2 are calculated, as f_x^{C1} and f_x^{C2}, respectively. Then two opposite-signed forces, $-f_x^{\mathrm{C1}}$ and $-f_x^{\mathrm{C2}}$, are uniformly added to all atoms in the two regions, respectively. In this way, the average atomic velocities and total atomic forces along the x direction in C1 and C2 become zero. It follows then that a constant velocity along the positive x direction, v_x^{A}, is applied to C1. Similar to the semi-rigid BC, atomic velocities and forces along the y and z directions are not constrained. It is necessary to put these boundary conditions together and then compare them, which may constitute a useful reference to researchers in the field.

For the constant applied stress loading mode, only the super-particle BC [22, 57] is imposed, to the best of our knowledge. Here, C1 and C2 are regarded as two super particles and their equations of motion are coupled with those of the atoms in other regions. This means that at each time step, the total force on each super particle is computed as the sum of the forces

on its constituent atoms. The coordinates and velocities of the atoms in each super particle are then updated so that each of C1 and C2 moves as a single entity. This is implemented by creating internal data structures for each super particle and performing inherent NVE time integration on these data structures. Meanwhile, positions and velocities of the constituent atoms are regenerated from the data structure in every time step and their comprehensive embodiment is the motion of super particle. In this way, each atom in each of the super particle has equal velocity and force. To exert a constant applied stress, we impose two constant, but different, forces, f_x^{A}, to each atom in region C1 and region C2, respectively. For C1, $f_x^{\mathrm{A}} = f_{\mathrm{C1}}^{\mathrm{A}}$ and is along the positive x direction; for C2, $f_x^{\mathrm{A}} = f_{\mathrm{C2}}^{\mathrm{A}}$ and is along the negative x direction. The resultant applied stress is then $N_{\mathrm{C1}} f_{\mathrm{C1}}^{\mathrm{A}}/(L_x L_y)$, which equals $N_{\mathrm{C2}} f_{\mathrm{C2}}^{\mathrm{A}}/(L_x L_y)$, where N_{C1} and N_{C2} are the total numbers of atoms in C1 and C2, respectively.

Besides loading mode and BCs, another important model setting is whether the temperature in a certain region is controlled via a thermostat. If it is, an NVT ensemble is used; otherwise, an NVE ensemble is used. In regions C1 and C2, atomic motions are associated with the BC; hence, an NVE ensemble is used there. When an NVT ensemble is applied to regions A, B1 and B2, we call it a 'full thermostat'; when an NVE ensemble is applied to all three regions, it is referred to as a 'no thermostat' case. As an intermediate case, we can apply an NVT ensemble to regions B1 and B2 and an NVE ensemble to region A. This case is called a 'partial thermostat'. It should be noted that 'partial thermostat' is a similar to 'stadium BCs' proposed and developed by Holian and Ravelo [74], Zhou *et al* [75], Holland and Marder [76], and Qu *et al* [77]. In both techniques, a specific region can be set for thermostat or temperature control. However, some discrepancies exist between them. Firstly, the stadium BCs can be applied to absorb energetic wave, while the partial thermostat cannot. Secondly, the stadium BC is a BC applied on the boundaries of the atomistic simulation cell, while the partial thermostat is independent of the BC and can be combined with different BCs, e.g., rigid, linear-rigid, semi-rigid and flexible BCs. As mentioned, the partial thermostat denotes that thermostat is only applied to a part of the interior region rather than the cell boundaries. In our simulations, no thermostat is used in the top or bottom layers, which are related to BCs. In comparison with the 'full thermostat', we opt to use the term 'partial thermostat' in this work for better readability and comparison. By combining the various types of BCs and thermostats for the two loading modes, we acquire nine sets of settings in total, which are summarized in table 2. Settings 1–6 are for the constant applied strain rate loading mode, while settings 7–9 are for the constant applied stress loading mode. Settings 1–4 identically have no thermostat, but different BCs. Settings 4–6 all use flexible BCs, but different thermostats. Settings 7–9 all use the super-particle BC, but different thermostats.

To study simulation cell size effects, six sets of edge lengths are studied, and these are listed in table 3. Models 1 and 2 are compared to assess whether the dislocation line length influences dislocation dynamics, while models 1, 3, and 4 aim to elucidate the effects of aspect ratio L_x/L_z. Here, the largest aspect ratio is 3.2 and the smallest is 0.8. Models 4–6 have the same aspect ratio but different values of L_x and L_z, whose influences will also be analyzed here. Here, it should be noted that Szajewski and Curtin investigated the spurious image stresses induced by dislocation bow-out around obstacles in MD simulations and compared the results with those in the multiscale image-free simulation conducted by the coupled atomistic/discrete dislocation method [78], in which they found the spurious image stress is minimum when the optimum aspect ratio (0.8) is applied. Since this is a benchmarking study, we compare the optimum aspect ratio (i.e., 0.8) and some non-optimum ones in order to provide a complete understanding of the aspect ratio effect, namely, how the non-optimum aspect ratios may affect the stress–strain

Table 2. Different modeling parameters used in this paper. Settings 1–6 are for the constant applied strain rate loading mode, while settings 7–9 for the constant applied stress loading mode. When a thermostat is or is not used in a region, an NVT or an NVE ensemble is used, respectively. In C1 and C2, no thermostat is used.

Setting	Loading mode	BC in C1(C2)	Thermostat in B1(B2)	Thermostat in A
1	Constant applied strain rate	Rigid	No	No
2		Linear-rigid	No	No
3		Semi-rigid	No	No
4		Flexible	No	No
5		Flexible	Yes	Yes
6		Flexible	Yes	No
7	Constant applied stress	Super-particle	No	No
8		Super-particle	Yes	Yes
9		Super-particle	Yes	No

Table 3. Edge lengths of the simulation cells used in this paper. Models 1 and 2 are compared to assess whether the dislocation line length influences dislocation dynamics, while models 1, 3, and 4 are to illustrate the effects of the aspect ratio L_x/L_z. Models 4–6 have the same aspect ratio, but different values of L_x and L_z.

Model	L_x (nm)	L_y (nm)	L_z (nm)
1	64	10	20
2	64	20	20
3	48	10	26.7
4	32	10	40
5	24	10	30
6	50	10	62.5

response of dislocation mobility without dislocation bow-out and dislocation–void interaction.

In the present simulations, different settings are utilized in these models, so that a particular series of combinations are obtained. Here, we use 'S + number + M + number' to denote the combinations. For example, 'S1M1' refers to the combination of setting 1 and model 1. For dislocation–void interaction, 'void' is added to the name, e.g., 'S1M1-void'. In addition, the letter 'e' is used in the notation of strain rate, e.g., '5e6' represents 5×10^6 s^{-1}. For the partial thermostat, the stress, e.g., the one in the stress–strain curve, is calculated by averaging atomic virial stresses in region A. For other thermostats, the stress is obtained by averaging atomic virial stresses in regions A, B1, and B2. For different thermostat cases, temperature in temperature–time curve is calculated in the same region as stress does. Unless stated otherwise, the term 'stress' refers to the internal stress of the simulation cell, instead of the 'applied stress' imposed by the surface traction, e.g., in the constant applied stress loading mode. In what follows, the amplitude of oscillations is the peak-to-peak amplitude. We let the average atomic displacements along the x direction in C1 and C2 be D_x^{C1} and D_x^{C2} in the constant applied stress loading mode, respectively. The corresponding strain is calculated as $(D_x^{C1} - D_x^{C2})/(L_z - 2L_C)$, and the strain rate is obtained accordingly. To visualize the dislocation, we use the polyhedral template matching method [79] implemented in OVITO [80]. By tracing the position of the leading partial dislocation, the dislocation displacement is determined.

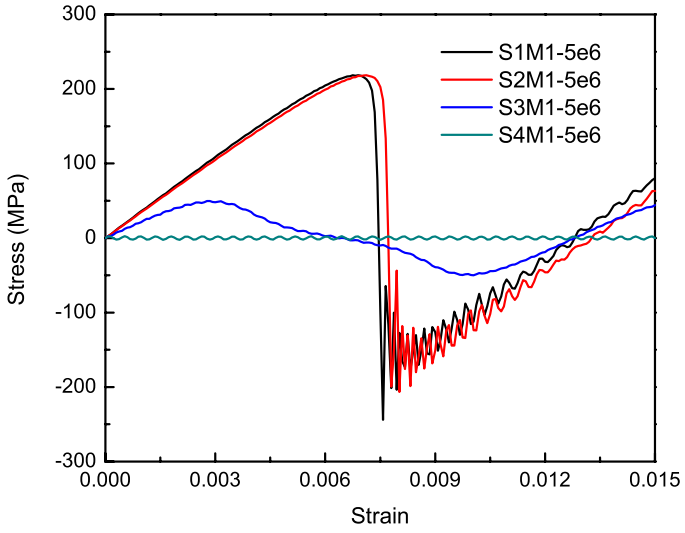

Figure 2. Shear stress–strain curves for S1M1, S2M1, S3M1 and S4M1 at a strain rate of 5×10^6 s^{-1}. S1: rigid boundary condition with no thermostat in B1 (B2) and A; S2: linear-rigid boundary condition with no thermostat in B1 (B2) and A; S3: semi-rigid boundary condition with no thermostat in B1 (B2) and A; S4: flexible boundary condition with no thermostat in B1 (B2) and A. M1: the simulation cell with 64 nm $\times$ 10 nm $\times$ 20 nm.

3. Dynamics of an edge dislocation

3.1. Constant applied strain rate loading mode: effects of the boundary condition

First, we study the effects of BCs on the stress–strain response under the constant applied strain rate loading mode. To this end, four cases are considered: S1M1, S2M1, S3M1, and S4M1. A strain rate of 5×10^6 s^{-1} is applied. When the simulation cell is subject to a simple shear, the dislocation keeps still until the shear stress reaches a critical level, which is conventionally defined as the Peierls stress [81, 82]. During the dislocation motion, periodic oscillations are observed in stress–strain curves for all BCs. Specifically, the semi-rigid BC (S3M1) results in an intermediate amplitude ($\sim$ 100 MPa), while rigid BC (S1M1) and linear-rigid BC (S2M1) are associated with the largest amplitude ($\sim$ 440 MPa), suggesting that latter two BCs are practically similar (figure 2).

The development of relatively large periodic stress oscillations, when using non-flexible BCs, have already been reported in the literature. In referemce [39], where the semi-rigid BC is utilized, the stress oscillations were attributed to the intrinsic inertia involved in fast dislocation motion. Interestingly, Krasnikov and Mayer [83] observed the oscillations only when the dislocation passes across the periodic BCs, which is contrary to the current work and to reference [39]. Rodney [61] considered that these oscillations resulted from the mismatch between the displacement profile in C1 (and C2) and the dislocation motion in the remaining regions. This mismatch yields a configurational force on the moving dislocation. To balance this force, while maintaining the dislocation motion at a constant speed, the internal stress needs to vary periodically with dislocation position.

The large stress oscillations are not physical and so should be minimized. Among the four BCs, the flexible BC has negligible stress amplitude ($\sim$ 6 MPa). In addition, its period of stress

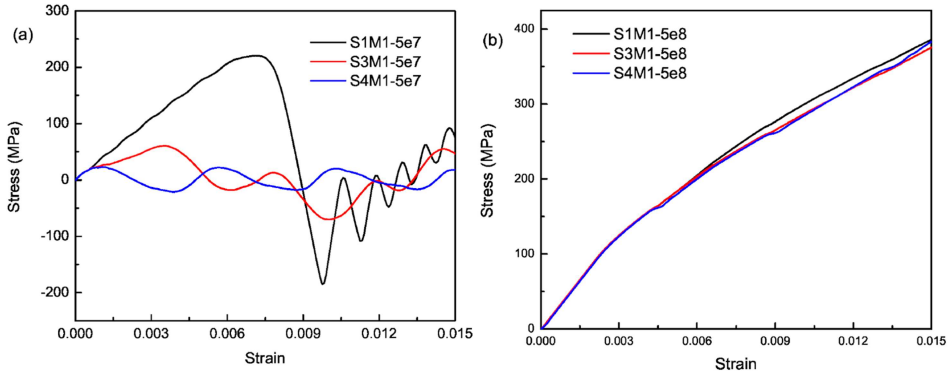

Figure 3. Shear stress–strain curves for S1M1, S3M1, and S4M1 at strain rates of (a) 5×10^7 s^{-1} and (b) 5×10^8 s^{-1}. S1: rigid boundary condition with no thermostat in B1 (B2) and A; S3: semi-rigid boundary condition with no thermostat in B1 (B2) and A; S4: flexible boundary condition with no thermostat in B1 (B2) and A. M1: the simulation cell with 64 nm $\times$ 10 nm $\times$ 20 nm.

oscillations is much shorter and the serrations correspond to the overcoming of the periodic Peierls barrier by the dislocation. Indeed, the flexible BC allows for atomic relaxation in C1 and C2 along all three directions, significantly reducing the mismatch between the motion of the surface region and the motion of dislocation.

To assess the effects of strain rate in conjunction with the BC, we use two higher strain rates in S1M1, S3M1, and S4M1. As shown in figure 3, at 5×10^7 s^{-1}, the rigid BC (S1M1) and flexible BC (S4M1) still possess the largest and smallest stress oscillation amplitudes, respectively. However, at a higher strain rate of 5×10^8 s^{-1}, the differences among BCs almost disappear. This outcome suggests that the choice of BC plays a more important role at lower strain rates. Tang [39] postulated that at high strain rates, the material deforms at rates that are too high for the dislocation motion to accommodate, characterized by an increasing stress rather than an oscillating one. Consequently, the influence of BCs can be overshadowed by that of the strain rate.

Further, to investigate the effect of simulation cell size, we compare models 1–6 with the semi-rigid BC, i.e., from models S3M1 to S3M6. The results are displayed in figure 4(a). Compared with S3M1, S3M2 has twice the dislocation line length. However, the stress–strain curves of S3M1 and S3M2 coincide, suggesting that the dislocation line length does not determine the macroscale stress fluctuations. Models S3M1, S3M3, and S3M4 have the same volume but different aspect ratios L_x/L_z. Models 4–6 have the same aspect ratio but different values of L_x and L_z. Results show that a smaller aspect ratio leads to a lower stress oscillation amplitude, while the values of L_x and L_z do not significantly affect the amplitude, as long as the ratio L_x/L_z remains the same. There is also an amplitude convergence in the models 4–6 with the same optimal aspect ratio $L_x/L_z = 0.8$ and different L_x (or L_z). In addition, the period of stress oscillation increases with the increase of the aspect ratio. Consistent with these results, Tang [39] found that doubling L_x, thereby increasing the aspect ratio L_x/L_z, caused the amplitude and the period of these stress oscillations to increase. Szajewski and Curtin [78] also pointed out that increasing the system size proportionally while keeping the aspect ratio constant does not affect the normalized image stress. Even for the non-optimal aspect ratio, convergence still exists with increasing sizes, but to the incorrect value of shear stress.

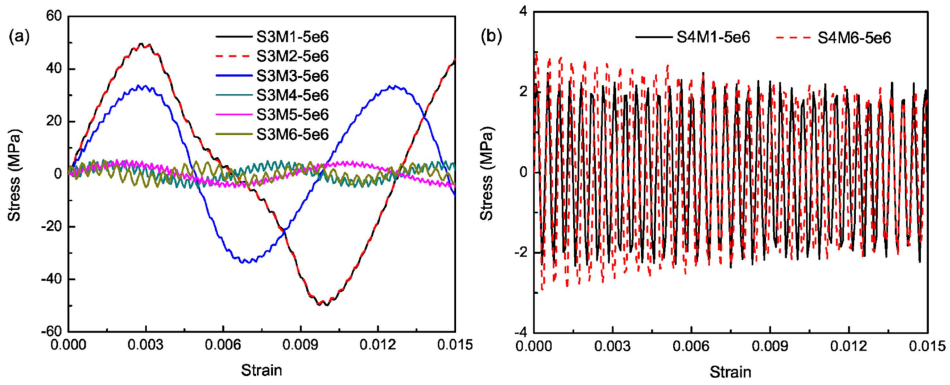

Figure 4. Shear stress–strain curves for (a) S3M1-S3M6 and (b) S4M1 and S4M6 at a strain rate of $5 \times 10^6\,s^{-1}$. S3: semi-rigid boundary condition with no thermostat in B1 (B2) and A; S4: flexible boundary condition with no thermostat in B1 (B2) and A. M1–M6 represent the simulation cells with 64 nm × 10 nm × 20 nm, 64 nm × 20 nm × 20 nm, 48 nm × 10 nm × 26.7 nm, 32 nm × 10 nm × 40 nm, 24 nm × 10 nm × 30 nm and 50 nm × 10 nm × 62.5 nm, respectively.

For the semi-rigid BC, models S3M1 and S3M6 differ the most. It is interesting to compare these two model sizes using the flexible BCs, i.e., S4M1 and S4M6. Figure 4(b) shows that only a small discrepancy occurs between the two sets when flexible BCs are used, suggesting the robustness of this BC. In what follows, flexible BCs will be used in all constant applied strain rate loading mode.

3.2. Constant applied strain rate loading mode: effects of the thermostat

Here, using model 6, we compare settings 4–6 to quantify the effects of whether or not, and which type of thermostat is applied, as shown in figure 5. At a low strain rate of $5 \times 10^6\ s^{-1}$, there is almost no difference among S4M6, S5M6, and S6M6 in the stress–strain curve and the dislocation displacement–time curve. The temperature–time curves differ among the three settings, yet the oscillation amplitude is very small (< 0.004 K), even in S4M6, which uses no thermostat. At a higher strain rate of $5 \times 10^7\ s^{-1}$, both stress–strain curve and dislocation displacement–time curve are still almost the same among the three settings. The temperature–time curve, however, has a larger oscillation amplitude (~ 0.07 K) if no thermostat is applied to region A. Also note that the period of stress oscillation increases with the strain rate. This finding suggests that applying no thermostat to region A, which enables a better representation of dislocation dynamics, does not result in a large increase in the temperature, as long as the strain rate is relatively low.

3.3. Constant applied stress loading mode: effects of the thermostat

As mentioned earlier, when the model uses constant applied stress loading, only the super-particle-rigid BC is utilized. Here, we study the effects of the thermostat, by comparing S7M6, S8M6, and S9M6, at a constant applied stress of 150 MPa. Figure 6 presents the results of this comparison. It is found that the calculated stress in the S9M6 simulation converges to the target value, i.e, 150 MPa, much faster than the stress in the S7M6 and S8M6 simulations.

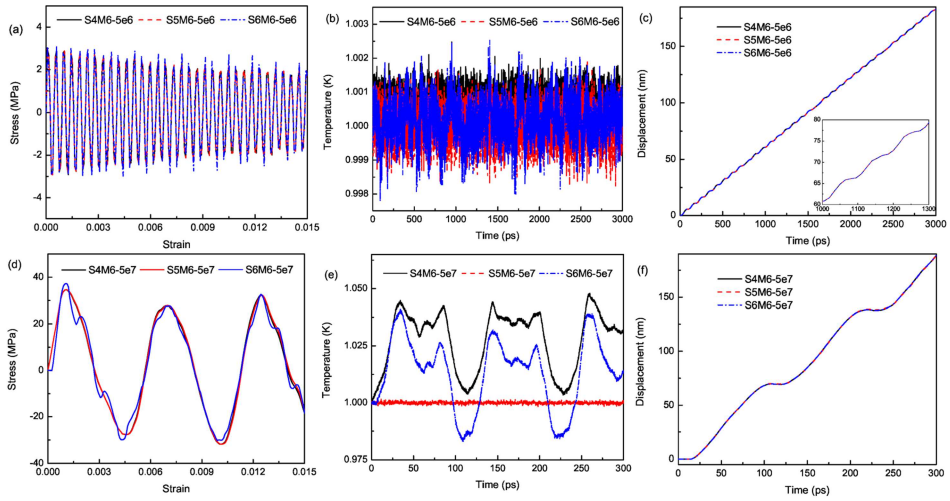

Figure 5. (a) Stress–strain, (b) temperature–time, and (c) dislocation displacement–time curves for S4M6, S5M6, and S6M6 at the strain rate of 5×10^6 s^{-1}. The corresponding results for a strain rate of 5×10^7 s^{-1} are shown in (d)–(f), respectively. S4: flexible boundary condition with no thermostat in B1 (B2) and A; S5: flexible boundary condition with thermostat in B1 (B2) and A; S6: flexible boundary condition with thermostat in B1 (B2) and no thermostat in A. M6: the simulation cell with 50 nm $\times$ 10 nm $\times$ 62.5 nm.

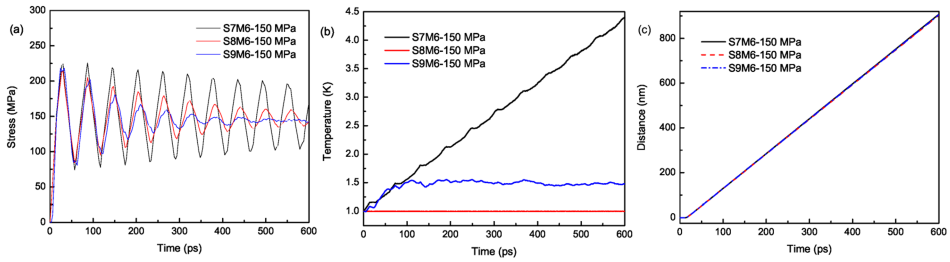

Figure 6. The evolution of (a) stress, (b) temperature, and (c) dislocation displacement with time for S7M6, S8M6, and S9M6 at a constant applied stress of 150 MPa. S7: super-particle boundary condition with no thermostat in B1 (B2) and A; S8: super-particle boundary condition with thermostat in B1 (B2) and A; S9: super-particle boundary condition with thermostat in B1 (B2) and no thermostat in A. M6: the simulation cell with 50 nm $\times$ 10 nm $\times$ 62.5 nm.

Regarding temperature, we observe that it increases near-linearly for S7M6, while the temperature evolution for S8M6 or S9M6 eventually converges to a stable value. An applied stress of 150 MPa results in an average strain rate of more than $5 \times 10^8\,s^{-1}$, which causes rapid temperature rise. This outcome suggests that it is necessary to apply a thermostat in the constant applied stress loading mode, due to the related high strain rate. Therefore, to alleviate the artificial friction on the dislocation, a partial thermostat, i.e., setting 9 as designated in this study, is recommended in the constant applied stress loading mode. As a final note, at the same simulation time, the dislocation displacements are almost the same in the three settings.

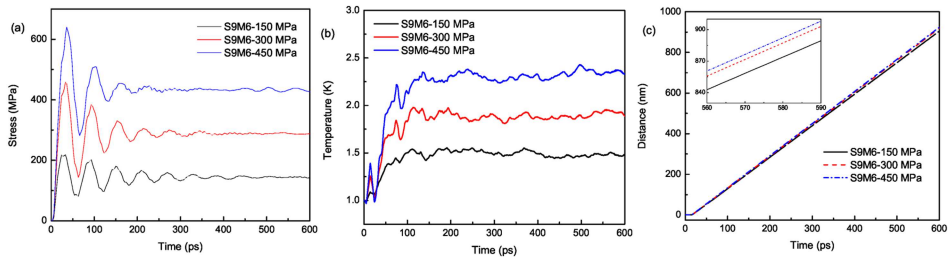

Figure 7. The evolution of (a) stress, (b) temperature, and (c) dislocation displacement with respect to time for S9M6 at a constant applied stresses of 150 MPa, 300 MPa, and 450 MPa, respectively. S9: super-particle boundary condition with thermostat in B1 (B2) and no thermostat in A. M6: the simulation cell with 50 nm $\times$ 10 nm $\times$ 62.5 nm.

3.4. Constant applied stress loading mode: effects of the applied stress

Next, we use S9M6 to study dislocation dynamics at different applied stress levels, including 150, 300, and 450 MPa. Figure 7 compares the time evolution of stress, temperature and dislocation displacement for these levels. As the applied stress increases, (i) the stress converges to the respective target value faster, (ii) the temperature eventually reaches a higher stable value, and (iii) the dislocation moves faster. Although the stable temperature, after controlling, rises with the increase of applied stress, these temperature rises are small (< 2 K). We also note that even at an initial temperature of 300 K, the temperature increase is no more than 1 K at an applied stress of 150 MPa. All these cases indicate that setting 9 behaves well for various applied stress.

4. Dislocation–void interactions

4.1. Constant applied strain rate loading mode

Similar to the dynamics of a dislocation, two loading modes—with constant applied strain rate or constant applied stress—can be used in the dislocation–void interactions. Here, we study the effects of the BC on the results of the interaction in the constant applied strain rate mode, using S1M1, S3M1, and S6M1. It is found that the stress–strain curves coincide with their counterparts in dislocation dynamics until the dislocation contacts the void. As time progresses in simulation the stress continues to rise until the dislocation cuts through the void, after which the stress drops rapidly. The critical stresses for the dislocation to break away from the void are denoted by the solid arrow in figure 8. We find that the critical stress depends on the model setting and increases in the order of S6M1, S3M1, and S1M1, which follows the order of the stress oscillation amplitude in these three cases. The important result here is that compared with the flexible BC, the rigid and semi-rigid BCs may predict a higher critical stress for dislocation–void interactions.

Since different strain rates and temperatures are often applied in dislocation–void interaction simulations, we investigate these two effects in S6M6, as shown in figure 9. As in figure 8, the solid arrows are used to point to the critical dislocation bypass stresses. Except in the case with the highest strain rate of $5 \times 10^8\,\mathrm{s}^{-1}$, all other cases experience a drop in the stress after the dislocation breaks away from the void. Thus, the stress increase induced by a high strain rate (e.g., $5 \times 10^8\,\mathrm{s}^{-1}$) dominates both dislocation dynamics and dislocation–void interaction. Below a critical strain rate ($10^7\,\mathrm{s}^{-1}$), the resulting stress–strain curves have much less fluctuations and the critical stresses converge at both 1 K and 300 K. In addition, when the strain rate

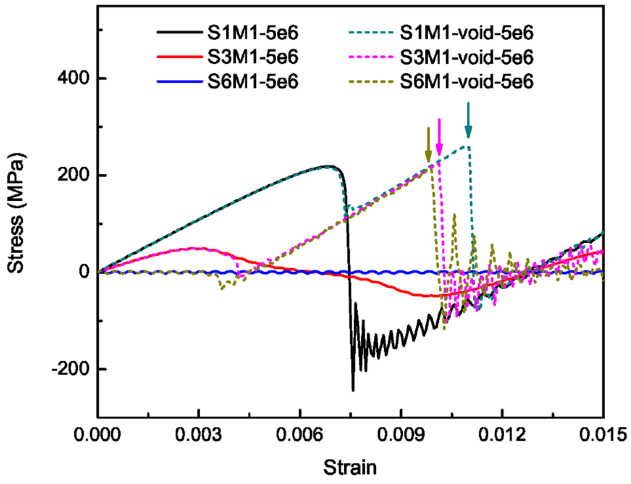

Figure 8. Shear stress–strain curves for S1M1, S3M1, and S6M1, and their counterparts in dislocation–void interaction cases. The solid arrows denote the critical stresses to break away from the void. S1: rigid boundary condition with no thermostat in B1 (B2) and A; S3: semi-rigid boundary condition with no thermostat in B1 (B2) and A; S6: flexible boundary condition with thermostat in B1 (B2) and no thermostat in A. M1: the simulation cell with 64 nm × 10 nm × 20 nm.

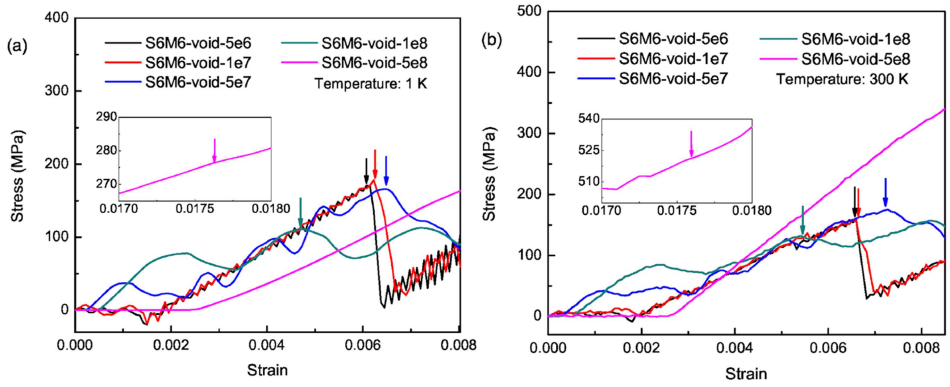

Figure 9. Shear stress–strain curve of S6M6-void at different strain rates and an initial temperature of (a) 1 K and (b) 300 K. The solid arrows denote the critical stresses for the dislocation to cut though the void. S6: flexible boundary condition with thermostat in B1 (B2) and no thermostat in A. M6: the simulation cell with 50 nm × 10 nm × 62.5 nm.

is higher than 10^7 s^{-1} and lower than 5×10^8 s^{-1}, the stress drop, if any, is relatively small after the dislocation bypasses the void. By contrast, the strain rates less than or equal to 10^7 s^{-1} result in a steep stress drop. Such a rapid drop is align with that in discrete dislocation dynamics simulations, in which the stress is largely released after the dislocation bypassing the obstacles [84]. All these indicate that the strain rate for dislocation–void interaction should be no greater than 10^7 s^{-1} in order to obtain reliable results. This critical strain rate (10^7 s^{-1}) is much

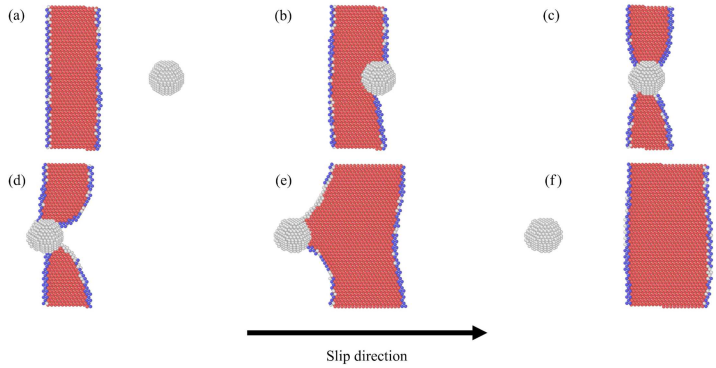

Figure 10. Atomic configurations at the shear strains of (a) 0.001 350, (b) 0.001 800, (c) 0.002 550, (d) 0.005 250, (e) 0.006 300 and (f) 0.006 375 in the case of S6M6-void with the strain rate of $10^7\,s^{-1}$ and an initial temperature of 1 K, respectively. In all the atomic configurations, body-centered cubic (BCC) atoms, hexagonal close-packed (HCP) atoms and those with unknown coordination structure are colored by blue, red and gray, respectively. Note that the void remains at the same location during the whole bypassing process. S6: flexible boundary condition with thermostat in B1 (B2) and no thermostat in A. M6: the simulation cell with 50 nm $\times$ 10 nm $\times$ 62.5 nm.

higher than those in most experimental condition which is an unavoidable issue for MD simulations due to the small timestep size. Nevertheless, MD simulations can still uncover important dislocation-mediated mechanisms at the nano-scale, which would be difficult in experiments.

It should be noted that the strain rate imposed in MD simulations is different from that in real material. The former has the elastic character and the latter behaves in more plastic form. In addition, the strain rate in MD simulations involves thermal activation events, which affect the critical stress to bypass void in our simulations and manifested by the strain rate dependence to some extent [85]. In addition, low and high strain rates in MD simulations can introduce inertial effects to different extents, while such an effect is absent in the real quasistatic experimental conditions. This effect is also confirmed in MD dislocation simulation with constant applied stress loading [86, 87], in which different applied stresses induce different strain rates. Given that the strain rate higher than $10^7\ s^{-1}$ is too high to obtain reliable results in dislocation–void interactions and the strain rate of $10^6\ s^{-1}$ is the lower bound in MD due to the limitation of the computational power, only a narrow strain rate range between $10^6\ s^{-1}$ and $10^7\ s^{-1}$ can be considered.

To better describe the dislocation–void interaction, we show the atomic configurations at different loading stages in the case of S6M6-void with the strain rate of $10^7\,s^{-1}$ and an initial temperature of 1 K. Dissociated into leading and trailing partials, the edge dislocation propagates initially upon shear loading along the slip direction on the glide plane (figure 10(a)). Then, the leading and trailing partial dislocations are sequentially pinned by the void, as shown in figures 10(b) and (c). With an increasing shear strain, the pinned leading partial dislocation bows out and breaks away from the void (figures 10(d) and (e)). Finally, the trailing partial dislocation is also unpinned and then the entire dislocation bypasses the void (figure 10(f)).

4.2. Constant applied stress loading mode

Last, we study the dislocation–void interactions using the constant applied stress loading mode at an initial temperature of 1 K. The critical applied stress is determined to be 70 ± 1 MPa.

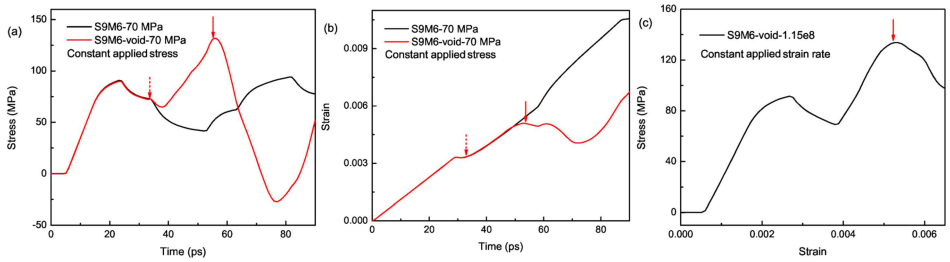

Figure 11. (a) Stress–time and (b) strain–time curves for S9M6 and S9M6-void at an applied stress of 70 MPa and an initial temperature of 1 K. (c) Stress–strain curve for S9M6-void at a strain rate of 1.15×10^8 s^{-1} and an initial temperature of 1 K. The dashed and solid arrows denote the stress at which the dislocation contacts the void and the critical stress when the dislocation breaks away from the void, respectively. S9: super-particle boundary condition with thermostat in B1 (B2) and no thermostat in A. M6: the simulation cell with 50 nm $\times$ 10 nm $\times$ 62.5 nm.

Although the applied stress is only 70 MPa, in studying the dynamics of the dislocation, the internal stress for S9M6 oscillates and may exceed 80 MPa. It takes some time for the internal stress to converge to a stable level, analogous to the plots in figure 7(a). As shown in figure 11(a), once the dislocation contacts the void, the stress–time curve of S9M6-void deviates from that of S9M6 and then rises up to 132 MPa, where the dislocation breaks away from void. On the other hand, the strain rate drops when the dislocation interacts with the void (figure 11(b)), indicating the interaction between the dislocation and the void can lower the strain rate in the constant applied stress loading mode. Before the dislocation contacts the void, the average strain rate is about 1.15×10^8 s^{-1}. For comparison, the stress–strain curve for S9M6-void in the constant applied strain rate loading mode with a strain rate of 1.15×10^8 s^{-1} is displayed in figure 11(c), in which the critical stress for the dislocation to bypass the void is found to be 133 MPa. This consistency implies both loading modes can be used to measure the critical dislocation for dislocation bypass. However, one difference exists in that the strain rate in the constant applied stress loading mode is associated with the applied stress and cannot be adjusted freely.

5. Conclusions

In this work, large-scale MD simulations are performed to investigate the effects of certain modeling parameters on dynamics of an edge dislocation and its interactions with a void in copper. The main conclusions are the following.

- Compared with rigid, linear-rigid and semi-rigid BCs, the flexible BC behaves better in the constant applied strain rate loading mode, characterized by its negligible stress oscillation as a dislocation moves in a lattice. As the strain rate increases, the discrepancy among these BCs vanishes. As the aspect ratio L_x/L_z increases, the stress fluctuations induced by the rigid BC become larger, while those by the flexible BC remain small.
- In both loading modes, the partial thermostat is advantageous over the full thermostat and no thermostat, because it can maintain the desired temperature, while not interfering with the dislocation motion.
- The BC plays an important role in both dislocation dynamics and dislocation–void interaction. In the constant applied strain rate loading mode, the flexible BC results in a much

smaller stress oscillation amplitude than non-flexible BCs including rigid, linear-rigid, and semi-rigid BCs. The stress oscillations induced by BCs during dislocation dynamics can result in a higher critical stress for the dislocation to bypass the void.

- At both low and high temperatures, the strain rate effect is significant in dislocation–void interaction. A strain rate of no more than 10^7 s^{-1} is recommended in order to achieve a converged result for the critical dislocation bypass stress.
- The constant applied stress loading mode is more suitable if one were to calculate the dislocation mobility, while the constant applied strain rate loading mode is better in the dislocation–void interaction cases. Both loading modes provide a consistent critical stress to cut through the void.
- Considering the optimum model settings affect similarly the dislocation motion and the stress release after bypassing in all dislocation–obstacle interactions, the conclusions for dislocation–void interaction problem, representing the optimum simulation settings, may also apply to more general dislocation–obstacle problems, involving different obstacle types and crystal structures, e.g., dislocation–precipitate, dislocation-Frank loop, and dislocation–stacking fault tetrahedron interactions in other FCC, BCC and HCP metals. Such optimum simulation settings include the flexible BC, the partial thermostat, lower strain rate (no higher than 10^7 s^{-1}), larger simulation cell and the optimum aspect ratio (0.8). The related LAMMPS files for dislocation–void interaction can be downloaded from https://github.com/wrj2018/MSMSE_2020.

Acknowledgments

We thank Prof. David Rodney for valuable discussions and suggestions. The work of W J was in part supported by the Regents in Mechanical Engineering Fellowship awarded by UC Santa Barbara. The work of S X was supported in part by the Elings Prize Fellowship in Science offered by the California NanoSystems Institute on the UC Santa Barbara campus. I J B acknowledges financial support from the National Science Foundation (NSF CMMI-1728224). Use was made of computational facilities purchased with funds from the National Science Foundation (CNS-1725797) and administered by the Center for Scientific Computing (CSC). The CSC is supported by the California NanoSystems Institute and the Materials Research Science and Engineering Center (MRSEC; NSF DMR 1720256) at UC Santa Barbara. This work used the Extreme Science and Engineering Discovery Environment (XSEDE), which is supported by National Science Foundation Grant Number ACI-1053575.

ORCID iDs

Wu-Rong Jian https://orcid.org/0000-0003-1712-1426
Min Zhang https://orcid.org/0000-0002-8227-2864
Shuozhi Xu https://orcid.org/0000-0003-0121-9445

References

[1] Anderson P M, Hirth J P and Lothe J 2017 *Theory of Dislocations* (Cambridge: Cambridge University Press)
[2] Chavoshi S Z and Xu S 2018 Temperature-dependent nanoindentation response of materials *MRS Commun.* **8** 15–28

[3] Chavoshi S Z and Xu S 2018 A review on micro- and nanoscratching/tribology at high temperatures: instrumentation and experimentation *J. Mater. Eng. Perform.* **27** 3844–58
[4] Saka H, Imura T and Yukawa N 1971 Measurement of the stress and strain on specimens in an electron microscope *Jpn. J. Appl. Phys.* **10** 1
[5] Raghothamachar B, Dhanaraj G, Bai J and Dudley M 2006 Defect analysis in crystals using x-ray topography *Microsc. Res. Tech.* **69** 343–58
[6] Xu S and Chen X 2019 Modeling dislocations and heat conduction in crystalline materials: atomistic/continuum coupling approaches *Int. Mater. Rev.* **64** 407–38
[7] Chavoshi S Z and Xu S 2019 Nanoindentation/scratching at finite temperatures: Insights from atomistic-based modeling *Prog. Mater. Sci.* **100** 1–20
[8] Farkas D, Frøseth A and Van Swygenhoven H 2006 Grain boundary migration during room temperature deformation of nanocrystalline Ni *Scr. Mater.* **55** 695–8
[9] Long X J, Wang L, Li B, Zhu J and Luo S N 2017 Shock-induced migration of $\Sigma 3\langle 110\rangle$ grain boundaries in Cu *J. Appl. Phys.* **121** 045904
[10] Zhang L, Lu C, Tieu K and Shibuta Y 2018 Dynamic interaction between grain boundary and stacking fault tetrahedron *Scr. Mater.* **144** 78–83
[11] Zhang L, Shibuta Y, Lu C and Huang X 2019 Interaction between nano-voids and migrating grain boundary by molecular dynamics simulation *Acta Mater.* **173** 206–24
[12] Chen D, Xu S and Kulkarni Y 2020 Atomistic mechanism for vacancy-enhanced grain boundary migration *Phys. Rev. Mater.* **4** 033602
[13] Yamakov V, Wolf D, Phillpot S R and Gleiter H 2002 Deformation twinning in nanocrystalline Al by molecular-dynamics simulation *Acta Mater.* **50** 5005–20
[14] Higginbotham A, Suggit M J, Bringa E M, Erhart P, Hawreliak J A, Mogni G, Park N, Remington B A and Wark J S 2013 Molecular dynamics simulations of shock-induced deformation twinning of a body-centered-cubic metal *Phys. Rev.* B **88** 104105
[15] Xu S, Su Y and Chavoshi S Z 2018 Deformation of periodic nanovoid structures in Mg single crystals *Mater. Res. Express* **5** 016523
[16] Yamakov V, Wolf D, Salazar M, Phillpot S R and Gleiter H 2001 Length-scale effects in the nucleation of extended dislocations in nanocrystalline Al by molecular-dynamics simulation *Acta Mater.* **49** 2713–22
[17] Spearot D E, Jacob K I and McDowell D L 2005 Nucleation of dislocations from [001] bicrystal interfaces in aluminum *Acta Mater.* **53** 3579–89
[18] Xu S and Su Y 2018 Dislocation nucleation from symmetric tilt grain boundaries in body-centered cubic vanadium *Phys. Lett.* A **382** 1185–9
[19] Zhang L, Mao W, Liu M and Shibuta Y 2020 Mechanical response and plastic deformation of coherent twin boundary with perfect and defective structures *Mech. Mater.* **141** 103266
[20] Xu S Z, Hao Z M, Su Y Q, Yu Y, Wan Q and Hu W J 2011 An analysis on nanovoid growth in body-centered cubic single crystalline vanadium *Comput. Mater. Sci.* **50** 2411–21
[21] Xu S and Su Y 2016 Nanovoid growth in BCC α-Fe: influences of initial void geometry *Modelling Simul. Mater. Sci. Eng.* **24** 085015
[22] Osetsky Y N and Bacon D J 2003 An atomic-level model for studying the dynamics of edge dislocations in metals *Modelling Simul. Mater. Sci. Eng.* **11** 427
[23] Bulatov V, Bulatov V V and Cai W 2006 *Computer Simulations of Dislocations* vol 3 (Oxford: Oxford University Press)
[24] Kim S, Ho D T, Kang K and Kim S Y 2016 Phonon scattering during dislocation motion inducing stress-drop in cubic metals *Acta Mater.* **115** 143–54
[25] Jin Z, Gao H and Gumbsch P 2008 Energy radiation and limiting speeds of fast moving edge dislocations in tungsten *Phys. Rev.* B **77** 094303
[26] Olmsted D L, Hector L G Jr, Curtin W A and Clifton R J 2005 Atomistic simulations of dislocation mobility in Al, Ni and Al/Mg alloys *Modelling Simul. Mater. Sci. Eng.* **13** 371
[27] Tsuzuki H, Branicio P S and Rino J P 2008 Accelerating dislocations to transonic and supersonic speeds in anisotropic metals *Appl. Phys. Lett.* **92** 191909
[28] Tsuzuki H, Branicio P S and Rino J P 2009 Molecular dynamics simulation of fast dislocations in copper *Acta Mater.* **57** 1843–55
[29] Weinberger C R 2010 Dislocation drag at the nanoscale *Acta Mater.* **58** 6535–41
[30] Higginbotham A, Bringa E M, Marian J, Park N, Suggit M and Wark J S 2011 Simulations of copper single crystals subjected to rapid shear *J. Appl. Phys.* **109** 063530

[31] Cho J, Molinari J-F and Anciaux G 2017 Mobility law of dislocations with several character angles and temperatures in fcc aluminum *Int. J. Plast.* **90** 66–75
[32] Krasnikov V S and Mayer A E 2018 Influence of local stresses on motion of edge dislocation in aluminum *Int. J. Plast.* **101** 170–87
[33] Gumbsch P and Gao H 1999 Dislocations faster than the speed of sound *Science* **283** 965–8
[34] Marian J, Cai W and Vasily V B 2004 Dynamic transitions from smooth to rough to twinning in dislocation motion *Nat. Mater.* **3** 158
[35] Queyreau S, Marian J, Gilbert M R and Wirth B D 2011 Edge dislocation mobilities in bcc Fe obtained by molecular dynamics *Phys. Rev.* B **84** 064106
[36] Verschueren J, Gurrutxaga-Lerma B, Balint D S, Sutton A P and Dini D 2018 Instabilities of high speed dislocations *Phys. Rev. Lett.* **121** 145502
[37] Groh S, Marin E B, Horstemeyer M F and Bammann D J 2009 Dislocation motion in magnesium: a study by molecular statics and molecular dynamics *Modelling Simul. Mater. Sci. Eng.* **17** 075009
[38] Fan H, Wang Q, Tian X and El-Awady J A 2017 Temperature effects on the mobility of pyramidal $\langle c + a \rangle$ dislocations in magnesium *Scr. Mater.* **127** 68–71
[39] Tang Y 2018 Uncovering the inertia of dislocation motion and negative mechanical response in crystals *Sci. Rep.* **8** 140
[40] Terentyev D, Bacon D J and Osetsky Y N 2008 Interaction of an edge dislocation with voids in α-iron modelled with different interatomic potentials *J. Phys.: Condens. Matter* **20** 445007
[41] Simar A, Voigt H-J L and Wirth B D 2011 Molecular dynamics simulations of dislocation interaction with voids in nickel *Comput. Mater. Sci.* **50** 1811–7
[42] Dutta A, Bhattacharya M, Gayathri N, Das G C and Barat P 2012 The mechanism of climb in dislocation–nanovoid interaction *Acta Mater.* **60** 3789–98
[43] Hayakawa S, Doihara K, Okita T, Itakura M, Aichi M and Suzuki K 2019 Screw dislocation–spherical void interactions in fcc metals and their dependence on stacking fault energy *J. Mater. Sci.* **54** 11509–25
[44] Shim J-H, Kim D-I, Jung W-S, Cho Y W, Hong K T and Wirth B D 2008 Atomistic study of temperature dependence of interaction between screw dislocation and nanosized bcc Cu precipitate in bcc Fe *J. Appl. Phys.* **104** 083523
[45] Liao M, Li B and Horstemeyer M F 2013 Interaction between prismatic slip and a $Mg_{17}Al_{12}$ precipitate in magnesium *Comput. Mater. Sci.* **79** 534–9
[46] Dérès J, Proville L and Marinica M-C 2015 Dislocation depinning from nano-sized irradiation defects in a bcc iron model *Acta Mater.* **99** 99–105
[47] Saroukhani S, Nguyen L D, Leung K W K, Singh C V and Warner D H 2016 Harnessing atomistic simulations to predict the rate at which dislocations overcome obstacles *J. Mech. Phys. Solids* **90** 203–14
[48] de Koning M, Kurtz R J, Bulatov V V, Henager C H, Hoagland R G, Cai W and Nomura M 2003 Modeling of dislocation–grain boundary interactions in fcc metals *J. Nucl. Mater.* **323** 281–9
[49] Chandra S, Samal M K, Chavan V M and Patel R J 2015 Atomistic simulations of interaction of edge dislocation with twist grain boundaries in Al-effect of temperature and boundary misorientation *Mater. Sci. Eng.* A **646** 25–32
[50] Chandra S, Samal M K, Chavan V M and Patel R J 2016 An atomistic study of resistance offered by twist grain boundaries to incoming edge dislocation in fcc metals *Mater. Lett.* **180** 11–4
[51] Fang Q and Sansoz F 2017 Influence of intrinsic kink-like defects on screw dislocation–coherent twin boundary interactions in copper *Acta Mater.* **123** 383–93
[52] Mordehai D, Ashkenazy Y, Kelson I and Makov G 2003 Dynamic properties of screw dislocations in Cu: a molecular dynamics study *Phys. Rev.* B **67** 024112
[53] Hatano T and Matsui H 2005 Molecular dynamics investigation of dislocation pinning by a nanovoid in copper *Phys. Rev.* B **72** 094105
[54] Wang Z Q and Beyerlein I J 2008 Stress orientation and relativistic effects on the separation of moving screw dislocations *Phys. Rev.* B **77** 184112
[55] Oren E, Yahel E and Makov G 2017 Dislocation kinematics: a molecular dynamics study in Cu *Modelling Simul. Mater. Sci. Eng.* **25** 025002
[56] Dutta A, Bhattacharya M, Barat P, Mukherjee P, Gayathri N and Das G C 2008 Lattice resistance to dislocation motion at the nanoscale *Phys. Rev. Lett.* **101** 115506

[57] Bacon D J, Osetsky Y N and Rodney D 2009 Dislocation–obstacle interactions at the atomic level *Dislocations in Solids* (Amsterdam: Elsevier) vol 15 pp 1–90
[58] Chen Z, Kioussis N and Ghoniem N 2009 Influence of nanoscale Cu precipitates in α-Fe on dislocation core structure and strengthening *Phys. Rev.* B **80** 184104
[59] Terentyev D, Bonny G, Domain C and Pasianot R C 2010 Interaction of a 1/2 $\langle 111 \rangle$ screw dislocation with Cr precipitates in bcc Fe studied by molecular dynamics *Phys. Rev.* B **81** 214106
[60] Osetsky Y N and Stoller R E 2015 Atomic-scale mechanisms of helium bubble hardening in iron *J. Nucl. Mater.* **465** 448–54
[61] Rodney D 2007 Activation enthalpy for kink-pair nucleation on dislocations: Comparison between static and dynamic atomic-scale simulations *Phys. Rev.* B **76** 144108
[62] Dang K, Bamney D, Bootsita K, Capolungo L and Spearot D E 2019 Mobility of dislocations in aluminum: Faceting and asymmetry during nanoscale dislocation shear loop expansion *Acta Mater.* **168** 426–35
[63] Plimpton S 1995 Fast parallel algorithms for short-range molecular dynamics *J. Comput. Phys.* **117** 1–19
[64] Mishin Y, Mehl M J, Papaconstantopoulos D A, Voter A F and Kress J D 2001 Structural stability and lattice defects in copper: *ab initio*, tight-binding, and embedded-atom calculations *Phys. Rev.* B **63** 224106
[65] Zhao F P, Li B, Jian W R, Wang L and Luo S N 2015 Shock-induced melting of honeycomb-shaped Cu nanofoams: Effects of porosity *J. Appl. Phys.* **118** 035904
[66] Jian W R, Li B, Wang L, Yao X H and Luo S N 2015 Shock response of open-cell nanoporous Cu foams: Effects of porosity and specific surface area *J. Appl. Phys.* **118** 165902
[67] Su Y and Xu S 2016 On the role of initial void geometry in plastic deformation of metallic thin films: A molecular dynamics study *Mater. Sci. Eng.* A **678** 153–64
[68] Xu S, Su Y, Chen D and Li L 2017 Plastic deformation of Cu single crystals containing an elliptic cylindrical void *Mater. Lett.* **193** 283–7
[69] Xu J, Xu S and Beyerlein I J 2019 Atomistic simulations of dipole tilt wall stability in thin films *Thin Solid Films* **689** 137457
[70] Xu S, Mianroodi J R, Hunter A, Beyerlein I J and Svendsen B 2019 Phase-field-based calculations of the disregistry fields of static extended dislocations in FCC metals *Philos. Mag.* **99** 1400–28
[71] Xu S, Smith L, Mianroodi J R, Hunter A, Svendsen B and Beyerlein I J 2019 A comparison of different continuum approaches in modeling mixed-type dislocations in Al *Modelling Simul. Mater. Sci. Eng.* **27** 074004
[72] Xu S, Xiong L, Chen Y and McDowell D L 2017 Validation of the concurrent atomistic-continuum method on screw dislocation/stacking fault interactions *Crystals* **7** 120
[73] Xu S, McDowell D L and Beyerlein I J 2019 Sequential obstacle interactions with dislocations in a planar array *Acta Mater.* **174** 160–72
[74] Holian B L and Ravelo R 1995 Fracture simulations using large-scale molecular dynamics *Phys. Rev.* B **51** 11275
[75] Zhou S J, Lomdahl P S, Thomson R and Holian B L 1996 Dynamic crack processes via molecular dynamics *Phys. Rev. Lett.* **76** 2318
[76] Holland D and Marder M 1999 Cracks and atoms *Adv. Mater.* **11** 793–806
[77] Qu S, Shastry V, Curtin W A and Miller R E 2005 A finite-temperature dynamic coupled atomistic/discrete dislocation method *Modelling Simul. Mater. Sci. Eng.* **13** 1101
[78] Szajewski B A and Curtin W A 2015 Analysis of spurious image forces in atomistic simulations of dislocations *Modelling Simul. Mater. Sci. Eng.* **23** 025008
[79] Larsen P M, Schmidt S and Schiøtz J 2016 Robust structural identification via polyhedral template matching *Modelling Simul. Mater. Sci. Eng.* **24** 055007
[80] Stukowski A 2010 Visualization and analysis of atomistic simulation data with OVITO–the open visualization tool *Modelling Simul. Mater. Sci. Eng.* **18** 015012
[81] Peierls R 1940 The size of a dislocation *Proc. Phys. Soc.* **52** 34
[82] Nabarro F R N 1947 Dislocations in a simple cubic lattice *Proc. Phys. Soc.* **59** 256
[83] Krasnikov V S and Mayer A E 2019 Dislocation dynamics in aluminum containing θ' phase: atomistic simulation and continuum modeling *Int. J. Plast.* **119** 21–42
[84] Lehtinen A, Granberg F, Laurson L, Nordlund K and Alava M J 2016 Multiscale modeling of dislocation-precipitate interactions in Fe: From molecular dynamics to discrete dislocations *Phys. Rev.* E **93** 013309

[85] Zhu T, Li J, Samanta A, Leach A and Gall K 2008 Temperature and strain-rate dependence of surface dislocation nucleation *Phys. Rev. Lett.* **100** 025502
[86] Bitzek E and Gumbsch P 2004 Atomistic study of drag, surface and inertial effects on edge dislocations in face-centered cubic metals *Mater. Sci. Eng.* A **387** 11–5
[87] Bitzek E and Gumbsch P 2005 Dynamic aspects of dislocation motion: atomistic simulations *Mater. Sci. Eng.* A **400** 40–4